NSRRC-J05257 (2016)

PCCP

PAPER

View Article Online
View Journal | View Issue

Published on 29 June 2016. Downloaded by Synchrotron Radiation Library on 17/08/2016 02:19:24.

Cite this: *Phys. Chem. Chem. Phys.*, 2016, 18, 20371

Relationships between the solution and solid-state properties of solution-cast low-*k* silica thin films†

Chao-Ching Chiang,[a] Chien-You Su,[b] An-Chih Yang,[a] Ting-Yu Wang,[c] Wen-Ya Lee,[d] Chi-Chung Hua*[b] and Dun-Yen Kang*[a]

Received 15th June 2016,
Accepted 28th June 2016

DOI: 10.1039/c6cp04166c

www.rsc.org/pccp

This paper reports on the fabrication of low-*k* (amorphous) silica thin films cast from solutions without and with two different types of surfactants (TWEEN® 80 and Triton™ X-100) to elucidate the relationships between the structural/morphological features of the casting solutions and the physical properties of the resulting thin films. Cryogenic transmission microscopy (cryo-TEM), static/dynamic light scattering (SLS/DLS), and small-angle X-ray scattering (SAXS) revealed contrasting colloidal dispersion states and phase behavior among the three casting solutions. Casting solution with the Triton™ X-100 surfactant produced stable (>90 days) nanoparticles with good dispersion in solution (mean particle size ~10 nm) as well as good mesopore volume (characterized by nitrogen physisorption) in powder and thin films of high mechanical strength (characterized by the nanoindentation test). The longer main chain and bulkier side units of the TWEEN® 80 surfactant led to stable micelle–nanoparticle coexisting dispersion, which resulted in the highest mesopore volume in powder and thin films with the lowest dielectric constant (~3) among the samples in this study. The casting solution without the surfactant failed to produce a stabilized solution or thin films of acceptable uniformity. These findings demonstrate the possibility of fine-tuning low-*k* silica film properties by controlling the colloidal state of casting solutions.

1. Introduction

Microporous and mesoporous silica thin films have been used in a wide range of applications involving the fabrication of bioactive coatings,[1,2] the surface modification of electrodes,[3] and the production of dielectric materials.[4] Processing schemes based on stabilized colloidal silica solutions for the fabrication of porous silica thin films can be implemented under moderate conditions and enable the engineering of solid-state properties by controlling the colloidal state of the casting solution.[5,6] One example is the siloxane-based solution processing of microporous silica thin films, which are promising membrane materials for applications involving molecular separation.[7–13]

The porosity of silica thin films can be controlled by adding structure directing agents (SDAs) to the casting solutions. SDAs help in the aggregation or polymerization of silica sol and in guiding the formation of micropores or mesopores in solid-state silica thin films.[14–18] Surfactants with long alkyl side chains, such as cetyltrimethylammonium chloride (CTAC)[19–21] and cetyltrimethylammonium bromide (CTAB),[22–24] are commonly used during the synthesis of SDAs to produce mesopores in silica thin films. Micropores in silica films can be produced using much smaller ionic SDAs, such as tetrapropylammonium hydroxide (TPAOH), which has been used in the fabrication of MFI-type pure-silica films.[25–29] The concentration of the SDA and aging time of the casting solution have also been shown to have a notable impact on the size of the pores in silica thin films.[30–36]

Porous silica films can be used as a layer with a low-dielectric constant (low-*k*) in electronic devices.[37–45] By definition, materials with a relative permittivity of less than 4 are referred to as low-*k* materials. Silica possesses a relative permittivity of approximately 4, whereas air has a value close to 1. Thus, porous silica films composed of silica and air (vacancies in the films are filled with air) make ideal low-*k* materials. Solution-processed crystalline microporous silica (*i.e.*, zeolite) films have been widely studied as low-*k* thin films, and a number of zeolite frameworks, including MFI,[46–48] MEL,[49–53] LTA,[54–56] and BEA,[57,58] have been explored. Despite the uniform periodic micropores of zeolite thin-films, high crystallinity often leads to undesirable cracks in thin films resulting in low mechanical strength and high leakage current.[59–61] Non-crystalline silica films have also been investigated

[a] *Department of Chemical Engineering, National Taiwan University, Taipei 10617, Taiwan, Republic of China. E-mail: dunyen@ntu.edu.tw*
[b] *Department of Chemical Engineering, National Chung Cheng University, Chia-Yi 62102, Taiwan, Republic of China. E-mail: chmcch@ccu.edu.tw*
[c] *Electron Microscope Unit of Instrument Center, National Taiwan University, Taipei 10617, Taiwan, Republic of China*
[d] *Department of Chemical Engineering and Biotechnology, National Taipei University of Technology, Taipei 10608, Taiwan, Republic of China*

† Electronic supplementary information (ESI) available: Angular dependencies, decay time distributions, OM images and XRD patterns of colloidal silica solutions, powders and thin films. See DOI: 10.1039/c6cp04166c

Published on 29 June 2016. Downloaded by Synchrotron Radiation Library on 17/08/2016 02:19:24.

in an effort to overcome the limitations associated with crystalline silica films. Appropriate surfactants can be used for this purpose to stabilize colloidal silica solutions during film casting and thus produce silica thin films with high porosity and consequently low relative permittivity and high mechanical strength.[62–65] However, the relationships between the solution-state properties and corresponding performances of the thin film have yet to be fully elucidated. A deeper understanding of this issue could certainly help to advance solution-processing techniques used for the fabrication of low-*k* silica thin films.

In this study, we sought to elucidate the effects of various casting solutions on the properties of the resulting thin films. We prepared a representative set of colloidal silica solutions for casting low-*k* silica thin films using two types of surfactants, TWEEN® 80 and Triton™ X-100, for the stabilization of silica colloids. A number of solution-state characterization techniques, including cryogenic transmission microscopy (cryo-TEM), static/dynamic light scattering (SLS/DLS), and small-angle X-ray scattering (SAXS), were used to reveal the structural/morphological features of the colloidal silica solutions prepared with and without the surfactant. Solid-state characterization included optical microscopy (OM), scanning electron microscopy (SEM), nitrogen physisorption, and nanoindentation. Thin-film-based devices were also fabricated to measure the dielectric constants and mechanical strength of silica thin films. Establishing the correlation between solution-state characteristics and the dielectric and mechanical properties of the thin films made it possible to engineer the dielectric performance of solution-processed low-*k* silica thin films through precise control of the colloidal state of the casting solutions.

2. Experimental

2.1. Preparation of colloidal silica solutions

Tetrapropylammonium hydroxide (TPAOH), ethanol, tetraethyl orthosilicate (TEOS), and deionized water were mixed at a molar ratio of 0.35 : 5.6 : 1 : 12.2 with a total mass of 18.59 g. The mixture was transferred into a perfluoroalkoxy alkane (PFA) bottle with a maximum capacity of 100 mL and aged at 30 °C for 3 h. The solution was then transferred to a Teflon® lined autoclave with a maximum capacity of 180 mL, which was placed in an oven at 100 °C for 18 h. A clear stock solution of 10.36 g was thus obtained. A portion of the stock solution (3.85 g) was mixed with ethanol of the same mass under stirring at 30 °C for 3 h to form a casting solution without a surfactant. Another 3.15 g of the stock solution was mixed with ethanol of the same mass and the surfactant TWEEN® 80 at a TWEEN® 80-to-TEOS mass fraction of 0.82 : 1. The mixture was stirred at 30 °C for 3 h to form the casting solution with TWEEN® 80. The same procedure was adopted for the preparation of casting solution with the surfactant Triton™ X-100.

2.2. Preparation of porous silica powders and thin-films

The casting solutions were dried in an oven at 90 °C for 6 h to obtain powder samples. Prior to characterization, the powder samples were calcined in a furnace by increasing the temperature to 450 °C at an elevation rate of 1 °C per minute and then held at that temperature for 5 h.

Silicon wafers (1 1 0) with a thin layer of thermal oxide were cut into squares (approximately 2 cm × 2 cm) for use as substrates in the casting of porous silica films. The casting solutions were applied to the substrates in drops until the entire surface was covered with solution, whereupon the substrates were spun at 2600 rpm for 30 s using a spin coater. The samples were placed in a drying oven and baked at 160 °C for 1 h. The thin-film samples were placed in a furnace before increasing the temperature to 450 °C at an elevation rate of 1 °C per minute to be held at that temperature for 5 h.

2.3. Characterization of casting solutions

2.3.1. Cryo-TEM characterization. A FEI Vitrobot™ Mark IV controlled environment vitrification system (CEVS) with liquid nitrogen as a cryogen was used for the preparation of samples. The solution with TWEEN® 80 and that without surfactant were vitrified at a thickness of approximately 200 nm on a TEM grid with a lacy carbon film. A QUANTIFOIL® TEM grid was used for the sample solution with Triton™ X-100. A Philips/FEI Tecnai G2 120 kV LaB_6 TEM with cryo-TEM capability was used to image the samples, which were held at temperatures below −178 °C.

2.3.2. Optical microscopy (OM). OM images were obtained using a conventional microscope (Olympus) equipped with a high resolution digital camera (Olympus). Samples for OM characterization were prepared using a drop-casting method on a glass substrate, followed by natural drying at room temperature or fast drying at 100 °C for 90 min.

2.3.3. DLS and SLS. Measurements were performed using a laboratory-built multi-angle (30° ~ 140°) light scattering apparatus equipped with a polarized He–Ne laser (λ_0 = 632.8 nm) and Peltier thermal controller, as described elsewhere.[66,67] All light scattering measurements were conducted at 25 ± 0.1 °C. The DLS experiment provided data on the normalized intensity autocorrelation function, $g^{(2)}(q,t)$, which is related to the normalized field autocorrelation function, $|g^{(1)}(q,t)|$, using the Siegert equation: $g^{(2)}(q,t) = 1 + \beta|g^{(1)}(q,t)|^2$, where β ($0 < \beta < 1$) is the spatial coherence factor depending on the detection optics.[68,69] The scattering vector q is defined as $q = 4\pi n \sin(\theta/2)/\lambda_0$, where n is the refractive index of the solvent, θ is the scattering angle, and λ_0 is the wavelength of incident light under vacuum. The normalized field autocorrelation function can be analyzed according to the following relation:

$$|g^{(1)}(q,t)| = \int_0^\infty A(\tau)e^{-t/\tau}d\tau \quad (1)$$

where $A(\tau)$ is the intensity-weighted decay time distribution associated with the decay time constant τ, and the distribution function of a multi-mode relaxation process can be retrieved using the commercial software CONTIN.[70] Each relaxation

 This journal is © the Owner Societies 2016

Published on 29 June 2016. Downloaded by Synchrotron Radiation Library on 17/08/2016 02:19:24.

mode was characterized by the mean decay time, $\langle\tau_i\rangle$, as $\langle\tau_i\rangle = \sum_n A_{in}(\tau)\tau_{in} / \sum_n A_{in}(\tau)$, where index n sums the entire regime that has been assigned to the ith mode.

SLS data were obtained by measuring the average scattering intensities at various detection angles. The measured scattering intensity ($I_{solu}(q)$) was normalized using the relation $I(q) = (I_{solu}(q) - I_{solv}(q))/I_{solv}(q)$, where $I_{solv}(q)$ is the measured scattering intensity of the solvent in the same apparatus, which results in $I(q)$ for use in form-factor analysis. The form factor of a polydisperse system can be expressed as follows:

$$P(q) \equiv \frac{I(q)}{I(0)} = \frac{\int_0^\infty G_n(R)\alpha^2(R)P(qR)\mathrm{d}R}{\int_0^\infty G_n(R)\alpha^2(R)\mathrm{d}R} \quad (2)$$

where $I(0)$ is the zero-angle scattering intensity extrapolated using the Guinier method, $G_n(R)$ is the number-weighted distribution of the characteristic size R, $\alpha(R)$ is the polarizability, and $P(qR)$ is the form factor. The polarizability is proportional to the power-law of R as $\alpha(R) \propto R^\gamma$; for instance, $\gamma = 3$ and $P(qR) = [3(\sin(qR) - qR\cos(qR))/(qR)^3]^2$ for rigid spheres, as used in this work.

2.3.4. SAXS. SAXS measurements were carried out at the beamline 23A station of National Synchrotron Radiation Research Center (NSRRC) in Taiwan. The solutions were placed in a sample cell with two Kapton® polyimide windows separated by 2.5 mm. Measurements were performed at room temperature at an X-ray wavelength of 0.8267 Å. SAXS patterns were taken with a 300-s exposure time using a Pilatus 1M-F CCD detector with a sample-to-detector distance of 3584.279 mm. The acquired two-dimensional (2-D) SAXS patterns were processed into 1-D profiles using proprietary LabVIEW-based software developed by the station.

2.4. Characterization of porous silica powders

Nitrogen physisorption was used to characterize the microporosity and mesoporosity of the powder samples. The powder samples were degassed at 350 °C in a vacuum chamber at 10^{-3} Torr for 10 h prior to measurements. Physisorption measurements were conducted using a Micromeritics 3Flex surface characterization analyzer. Powder X-ray diffraction (XRD) was performed using a Rigaku diffractometer with Cu Kα radiation operating at 50 mA and 60 kV at a scan rate of 10° 2θ min^{-1}. The scanning range was from 5° to 30° 2θ with a step size of 0.02°.

2.5. Characterization of porous silica thin-films

Grazing-incidence X-ray diffraction (GIXRD) was performed on thin-film samples using a PANalytical X'pert diffractometer with a Cu Kα source and a scanning range from 5° to 30° 2θ at a step size of 0.02°. The thin-film samples were imaged using a digital camera (Sony Alpha NEX-6), a zoom stereo microscope (Olympus SZ-11 equipped with a microscope camera POTOP PMD-500), and scanning electron microscopes (Hitachi S-4800 and JOEL JSM 7600F operated under an accelerating voltage of 10 kV). Nanoindentation tests on the thin-film samples were conducted at room temperature using a Hysitron TI 950 TriboIndenter. A 13 μN per second loading/unloading rate and 5 second dwell-time were used in all nanoindentations. The indenter was equipped with a Berkovich (with a half angle of 65.3°) pyramidal diamond tip. The Young's modulus and hardness of the thin-film samples were deduced from the raw data of the nanoindentation tests. The capacitance of the thin-film samples was measured using a Keysight 4284A Precision LCR meter under a bias voltage of 1 V at frequencies of 1, 10, and 100 kHz, respectively. The relative permittivity (ε_r) of the thin films was calculated using the relation $\varepsilon_r = Cd/\varepsilon_0 A$, where C is the measured capacitance, d is the thickness (determined from cross-sectional SEM images), A is the area of the deposited electrode (2 mm^2), and ε_0 is the vacuum permittivity (8.854×10^{-12} F m^{-1}).

3. Results and discussion

3.1. Properties of colloidal casting solutions

3.1.1. Cryo-TEM characterization. Colloidal casting solutions were first characterized by cryo-TEM imaging, as shown in Fig. 1. Among the three solution samples in this study, the one with TWEEN® 80 produced the least agglomeration, which resulted in the smallest particles (Fig. 1b). The particles in this sample appeared to be coated by a "white ring," which is likely TWEEN® 80 on the surface of the silica nanoparticles. These features are indicative of good interaction between TWEEN® 80 and the silica colloids. The sample prepared using Triton™ X-100 (Fig. 1c) exhibited a somewhat higher degree of agglomeration, similar to the case without surfactant (Fig. 1a). The agglomeration was more severe, though, in the sample prepared without surfactant.

The mean particle diameters of the sample with TWEEN® 80, Triton™ X-100, and without a surfactant were 56.2, 47.4, 51.9 nm, respectively. This suggests that the addition of the surfactant had a marginal effect on the particle size. Nonetheless, it should be noted that the cryo-TEM results reveal mainly quasi-solution-state features, and the results do not describe the effects of aging. It is worth noting the chemical structures of TWEEN® 80 (Fig. 1d) and Triton™ X-100 (Fig. 1e). Both of these surfactants bear hydroxyl groups that bind to the surface of silica nanoparticles; however, TWEEN® 80 possesses a longer main chain and bulkier side units, which will be shown to greatly affect the colloidal state and thin-film properties. According to previous reports, both TWEEN® 80[62,71–73] and Triton™ X-100[74,75] could bind the silica surface through hydrogen bonds.

3.1.2. DLS/SLS/SAXS/OM characterization. SLS and DLS analyses, which have been successfully utilized to reveal the nucleation mechanisms[76–79] and nanoparticle interactions[80,81] in various colloidal silica solutions, were performed on fresh solution samples and those that underwent aging for 90 days to shed light on the cryo-TEM features and reveal the true colloidal state of the solutions. Fig. 2 presents SLS profiles of all three solutions. The fresh solution without surfactant and that prepared with Triton™ X-100 both were featureless, which suggests that the mean radius of gyration (R_g) of silica nanoparticles in these solutions was smaller than what might be resolved in the accessible q-range (*i.e.*, below 30 nm); see also the SAXS analysis discussed shortly. In contrast, the SLS profile of the fresh

Published on 29 June 2016. Downloaded by Synchrotron Radiation Library on 17/08/2016 02:19:24.

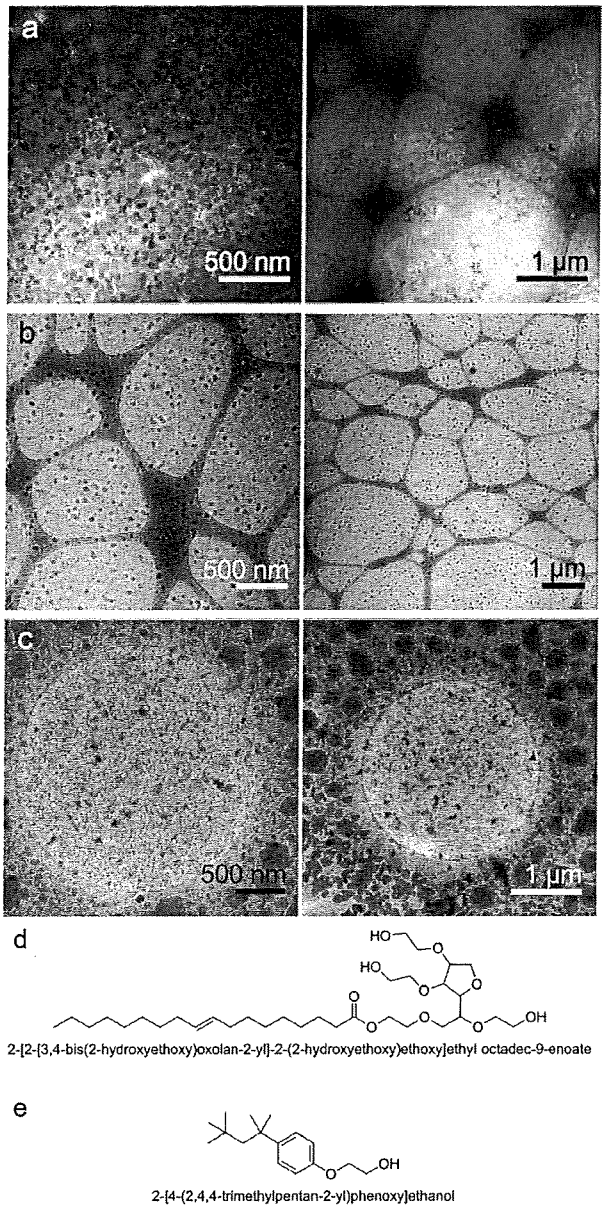

Fig. 1 Cryo-TEM images of casting solutions with (a) no surfactant, (b) TWEEN® 80, and (c) Triton™ X-100 as surfactant. Chemical structures and IUPAC names of (d) TWEEN® 80 and (e) Triton™ X-100.

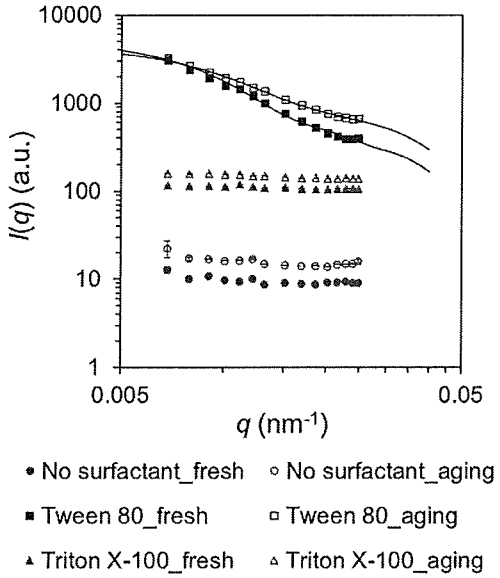

Fig. 2 SLS profiles of three casting solutions with no surfactant, TWEEN® 80, and Triton™ X-100 as surfactant. The intensity profiles of TWEEN® 80 and Triton™ X-100 have been rescaled vertically by a factor of 10 for clarity. The solid lines within TWEEN® 80 data represent the curves fitted using eqn (2) along with a form factor for spherical particles.

solution with TWEEN® 80 exhibited a notable q dependence that can be well described by the form factor of spherical particles, with $R_g \sim 226$ nm. All three of the aged samples exhibited only moderate changes in scattering intensity or the detailed profile.

Fig. 3 presents the DLS features, $g^{(1)}(q,t)$, over a range of scattering angles (left panels) and at the smallest scattering angle $\theta = 30$ (right panels). From the angular dependencies shown in the left panel of Fig. 3a, it can be seen that all DLS curves collapse on a master curve as the decay time is rescaled with q^2. This feature is indicative of the presence of a single diffusive mode and, accordingly, silica nanoparticles with a narrow size distribution. Using the standard Stokes–Einstein relation along with the mean decay rate extracted from the curve, the mean hydrodynamic radius was determined to be $R_H \sim 50$ nm. A similar feature can be noted for the solution with Triton™ X-100 (Fig. 3c). In contrast, the DLS curves for the solution with TWEEN® 80 (Fig. 3b) were clearly indicative of a broad distribution in R_H and, in particular, it appears to foster micrometer-sized aggregate species ($R_H \sim 1$ μm). For the aged solutions, the comparison shown in the right panels of Fig. 3 indicated that while the solution system utilizing either surfactant exhibited no appreciable change after aging for 90 days, the solution without surfactant changed drastically resulting in the formation of an abundance of micrometer-sized aggregates. The effectiveness of the two surfactants used in this study in stabilizing colloidal silica solution should be evident. On the other hand, both the SLS and DLS responses revealed that there is a notable difference in the mean particle size between the two solution systems utilizing different surfactants, which we discuss next.

We showed previously that well-dispersed, small silica nanoparticles can be observed in the cryo-TEM image of the solution with TWEEN® 80 (Fig. 1b). This observation is in interesting contrast to the SLS/DLS features above suggestive of the presence of much larger aggregate species in the same solution system. To resolve this seeming inconsistency, and to shed light on the disparity between the two solution systems utilizing different surfactants, we present in Fig. 4 the OM images of thin films produced from each of the three solutions using drop-casting and rapid drying (see also ESI,† Fig. S1, for results of films that underwent natural drying). A significant finding was that the morphological features of the TWEEN® 80 system (Fig. 4b)

This journal is © the Owner Societies 2016

Published on 29 June 2016. Downloaded by Synchrotron Radiation Library on 17/08/2016 02:19:24.

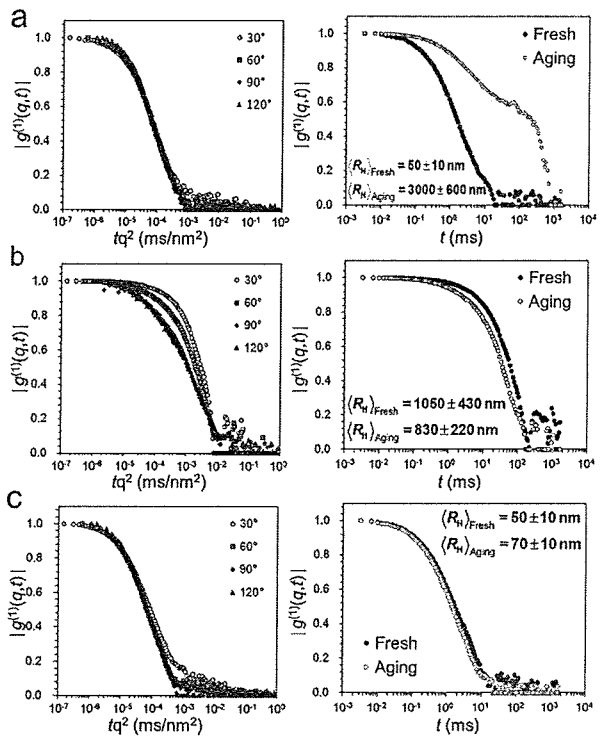

Fig. 3 Comparisons of field autocorrelation function and mean hydrodynamic radius R_H for fresh or aged solution with (a) no surfactant, (b) TWEEN® 80, and (c) Triton™ X-100 as surfactant.

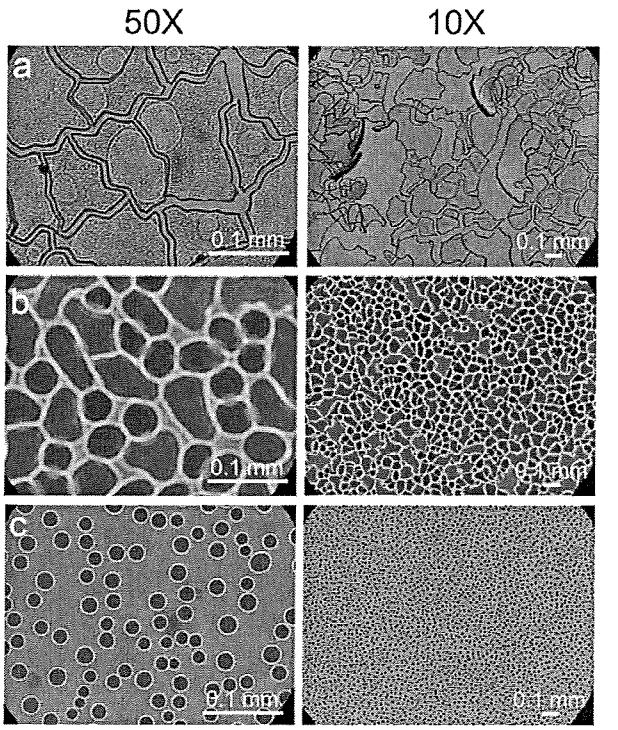

Fig. 4 OM images of fast-drying (100 °C for 90 minutes), drop-cast films produced from solutions with (a) no surfactant, (b) TWEEN® 80, and (c) Triton™ X-100 as surfactant.

suggested that, in addition to being adsorbed onto the silica nanoparticles, the (non-adsorbed) surfactant molecules might have associated to form micelles,[82–84] showing the coexistence of two distinct microphases (right panel: "dark" phase for silica nanoparticles and "light" phase for micelles) in quenching thin films. For comparison, the thin film produced from the solution with Triton™ X-100 (Fig. 4c) led to a more commonly observed state of particle dispersion. The contrasting OM images might, therefore, explain prior SLS and DLS analyses indicating the formation of large (micelle) species with $R_H \sim$ 1000 nm (or $R_g \sim$ 200 nm) in the solution with TWEEN® 80, while the other surfactant Triton™ X-100 might have little tendency to associate and the light scattering analyses basically reflect the mean size of silica nanoparticles. Presumably, the prodigious micelles formed in solution bear only low contrast with the solvent medium and therefore could become "invisible" in cryo-TEM imaging. Furthermore, the OM images in Fig. 4b and c indicated that silica agglomerates of size about 10 μm and greater may be produced in quenching thin films. The size differs substantially from what has been resolved in prior cryo-TEM imaging and a later SAXS analysis in the pristine solution state, *i.e.*, $R_g \sim$ 10 nm. These features underline the indispensability of analyzing schemes such as light scattering for an *in situ* characterization of solution-state properties.

Early studies on colloid–surfactant mixture systems suggested that colloidal interactions may be controlled through the coexisting surfactant micelles.[82–85] Herein, it is worth noting that the formation of nanoparticle thin films with a similar percolated state as observed in Fig. 4b could be advantageous in many scientific or practical applications, considering that such a structure would require relatively few seed particles to form a 3-D continuous pathway for subsequent applications involving electron conduction or gel incubation. Subsequent investigation, in fact, revealed that as a surplus amount of TWEEN® 80 was utilized, the silica solution turned into gel upon short-term (*i.e.*, about one day) aging at room temperature; see photos in ESI,† Fig. S2. A similar gel phase, however, was unobservable for the solution with Triton™ X-100.

Fig. 5 presents a comparison of SAXS profiles for the three solution systems. The solution with TWEEN® 80 exhibited a slight upturn at low q (*i.e.*, $q < 0.1$ nm^{-1}) indicative of the presence of large aggregate clusters. This feature is consistent with prior SLS analysis, which indicated a mean micelle size of $R_g \sim$ 200 nm. For the other solutions, the Guinier plots for the same q range yielded a mean particle size of $R_g \sim$ 10 nm, as shown in the inset figure; a more detailed fit of the full curve as presented in ESI,† Fig. S3, yielded a slightly larger particle size (*i.e.*, R_g = 15–20 nm). In the high-q region (*i.e.*, $q > 1$ nm^{-1}), the scaling exponent in $I(q) \sim q^{\alpha}$ can be utilized to reveal the (interior) fractal dimensions of silica nanoparticles, and values around 2 were found with the solution without surfactant and that with Triton™ X-100. This result is indicative of the cluster–cluster aggregation mechanism typical of colloidal particles, as previously found for silica precursor solutions using time-resolved light scattering techniques.[78,79] In contrast, the solution

Published on 29 June 2016. Downloaded by Synchrotron Radiation Library on 17/08/2016 02:19:24.

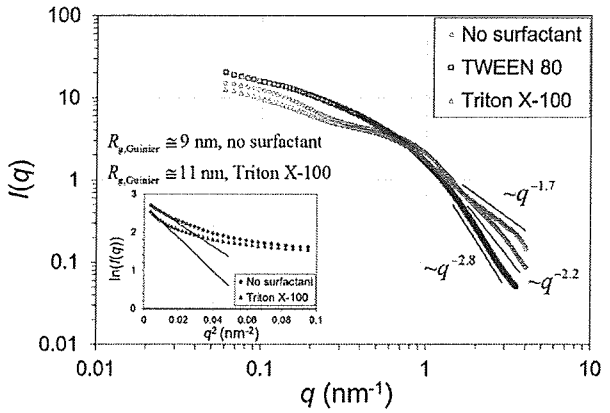

Fig. 5 SAXS profiles of solutions without surfactant, with TWEEN® 80, and Triton™ X-100 as surfactant, respectively. The inset presents the Guinier-plot fitting of the solution without surfactant and with Triton™ X-100, respectively.

with TWEEN® 80 possesses a nominal fractal dimension of about 3. Considering the size of micelle species in this solution system, one expects that the scattering profile in this region is primarily an indication of micelle surface properties with a predicted scaling law of $I(q) \sim q^{-4}$ in the so-called Porod regime. Thus, a scaling exponent of ~ -3 as has been observed with this solution system might be attributed to the combined effects of silica nanoparticles (with a scaling exponent of ~ -2) and surfactant micelles (with a scaling exponent of ~ -4).

In summary, SLS/DLS/SAXS analyses of the solution samples and OM images of the corresponding quenching films clearly revealed that the addition of Triton™ X-100 or TWEEN® 80 promotes the dispersion and stability of colloidal silica solution, yet with distinct mechanisms and structural/morphological features. The peculiar features as have been noted for the solution system using the bulkier surfactant TWEEN® 80, likely, have arisen from its tendency to associate and, subsequently, form large micelles. The detailed mechanism of micelle growth and, in particular, the interplay with silica nanoparticles in solution remain enigmatic, while the percolated, bi-continuous morphological feature noticed with the quenching thin film is appealingly attractive in its many potential applications including gel incubation. Bearing these features in mind, we next examine the porous, mechanical, and dielectric properties of the powder and thin-film samples produced from the three casting solutions.

3.2. Porosity of silica powders

Nitrogen physisorption was used to characterize the porosity of three powder samples produced from the casting solutions, the results of which are presented in Fig. 6. It should be mentioned that the powder XRD patterns (Fig. S4, ESI†) are basically featureless, which suggests that none of the powders in this study are crystalline in nature. However, a minor modification of the synthesis procedure presented in this work could lead to crystalline nanoporous materials, zeolite MFI.[63]

First, the isotherms in the low-pressure regime ($P/P_0 < 0.01$) of the three samples are nearly identical, which suggests the

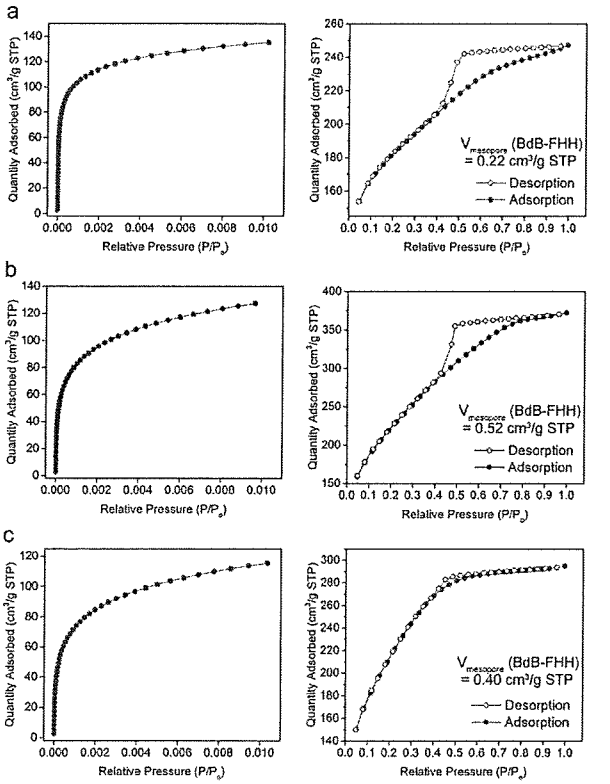

Fig. 6 Nitrogen physisorption isotherms of powder samples derived from solutions with (a) no surfactant, (b) TWEEN® 80, and (c) Triton™ X-100 as surfactant. The isotherms shown in the left column were obtained in the low-pressure regime, while those in the right pertain to the high-pressure regime.

existence of micropores in the silica nanoparticles in the three powder samples (pore size <2 nm). The micropores were likely created by the addition of tetrapropylammonium hydroxide (TPAOH) in the synthesis of silica colloids. Given that the same amount of TPAOH was used in all the three powder samples, the similarity in microporosity among them should not be too surprising. In the high-pressure regime ($P/P_0 > 0.1$), the isotherms in all three cases revealed hysteresis in the desorption curve, which is indicative of the existence of mesopores (2 nm < pore size <50 nm). The mesopores are believed to arise from the inter-particle spacing of agglomerated silica colloids, which are approximately ten nanometers in size, as determined in SLS/SAXS analyses of the solution samples. We derived the mesopore volumes in the powder samples from the raw isotherms using the BdB-FHH[86] model as follows: from the solution without surfactant (0.22 cm^3 g^{-1} STP), from the solution with TWEEN® 80 (0.52 cm^3 g^{-1} STP), and from the solution with Triton™ X-100 (0.40 cm^3 g^{-1} STP). The lowest mesopore volume (from the solution without surfactant) could be attributed to the compact nanoparticle aggregates in the sample. The addition of TWEEN® 80 more than doubled the mesopore volume by suppressing the agglomeration of silica nanoparticles in solution, as indicated by cryo-TEM and light scattering results.

This journal is © the Owner Societies 2016

Published on 29 June 2016. Downloaded by Synchrotron Radiation Library on 17/08/2016 02:19:24.

The powder sample fabricated from the solution with Triton™ X-100 also exhibited a notable increase in mesopore volume, although the effect was not as pronounced. The disparity in mesopore volume from the two surfactants might be ascribed to the micelle–colloid coexistence brought in by the use of TWEEN® 80, through a consequently more efficient packing of silica nanoparticles upon quenching. Determining whether this was instrumental in determining the mesopore volume in powder or film samples is an avenue worth pursuing in the future.

3.3. Properties of porous silica thin films

Three thin-film samples were prepared by spin casting the colloidal solutions on silicon wafers. Fig. 7 presents photographs and OM images of the resulting thin films. The thin film formed from the solution without surfactant presents a notable lack of uniformity on a length scale of millimeters. In contrast, the thin films cast from solutions with TWEEN® 80 or Triton™ X-100 present homogeneous morphologies at that scale.

As shown in Fig. 8, the microstructure of the thin film was investigated using SEM. Severe cracks can be clearly observed in the top-view image of the thin film produced from the solution without surfactant, whereas the other two thin films reveal relatively homogeneous top-surface morphologies. The uniformity of the two thin films cast from the solutions with surfactant was confirmed by cross-sectional SEM images, in which a uniform thin layer of ~260 nm can be clearly observed. Overall, the OM and SEM images of the solution-cast thin films in Fig. 7 and 8 seem to suggest that the thus promoted nanoparticle dispersion and stabilization in solution by the use of TWEEN® 80 or Triton™ X-100 have assisted in the fabrication of nanoscale thin films with a high degree of uniformity, as discussed in prior work.[87–92] Note also that the thin film prepared from the solution without a surfactant was the thinnest, which might be ascribed to the highest degree of agglomeration in solution and, consequently, the least efficient nanoparticle packing upon quenching—a similar feature that underlines the lowest mesopore volume in powder sample as discussed previously. As shown in ESI,† Fig. S5, GIXRD patterns confirm the results of XRD analysis indicating the non-crystalline nature of the three thin-film samples.

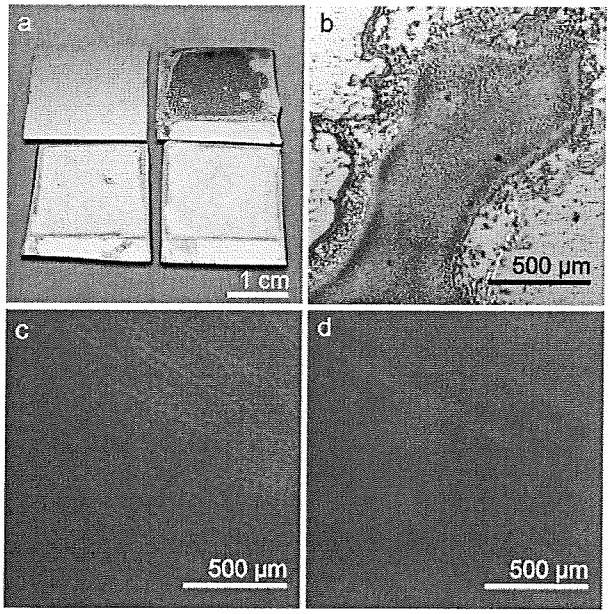

Fig. 7 (a) Photographs of bare silicon wafer (top left) and thin films cast from solutions with no surfactant (top right), with TWEEN® 80 (bottom left), and Triton™ X-100 (bottom right) surfactant. OM images of thin films cast from solutions with (b) no surfactant, (c) TWEEN® 80, and (d) Triton™ X-100 as surfactant.

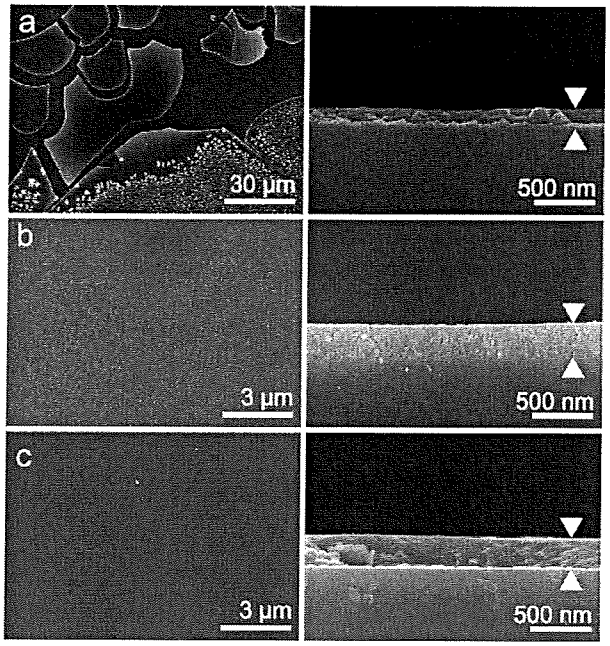

Fig. 8 SEM images of thin films cast from solutions with (a) no surfactant, (b) TWEEN® 80, and (c) Triton™ X-100 as surfactant. Top-view images appear in the left panels, while side-view images are shown on the right. The arrows indicate the location of the silica thin film deposited on the silicon wafer.

Due to the lack of uniformity in the thin film produced from the solution without surfactant, only the other two thin-film samples underwent further analysis using nanoindentation tests and measurements of dielectric constant. As shown in Fig. 9, the nanoindentation tests provided data from which to derive the Young's modulus and hardness of the thin films. The thin film obtained from the solution with Triton™ X-100 presents a higher Young's modulus and hardness than that cast from the solution with TWEEN® 80. This can be explained by the fact that the sample with TWEEN® 80 possesses a bi-continuous phase and, consequently, a larger mesopore volume. The presence of mesopores presumably weakens the mechanical strength of the materials.

Fig. 10 lists the dielectric constants (ε_r) of the two thin-films measured at frequencies of 1, 10, and 100 kHz, respectively. At all tested frequencies, the values of the thin-film cast from the solution with TWEEN® 80 are far below those of the sample with Triton™ X-100. It has previously been demonstrated that

Published on 29 June 2016. Downloaded by Synchrotron Radiation Library on 17/08/2016 02:19:24.

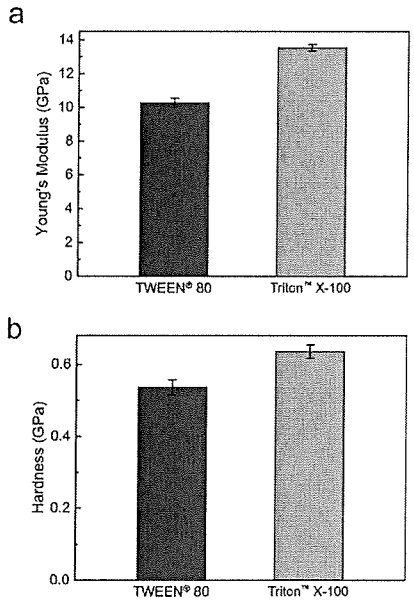

Fig. 9 (a) Young's modulus and (b) hardness of thin films cast from solutions with TWEEN® 80 and Triton™ X-100 as surfactants, respectively.

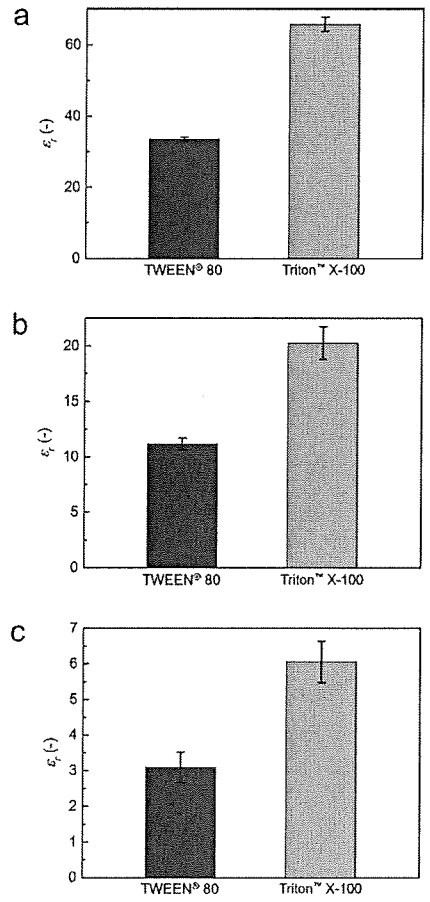

Fig. 10 Dielectric constants measured at frequencies of (a) 1, (b) 10, or (c) 100 kHz for thin films cast from solutions with TWEEN® 80 and Triton™ X-100 as surfactants, respectively.

porosity (particularly mesoporosity) can greatly reduce the ε_r value of thin-film materials.[62,63] Thus, these results are consistent with mechanical properties, both of which depend largely on the mesopore volume of the thin film. At an operating frequency of 100 kHz, the ε_r value of the TWEEN® 80-based thin film was approximately 3, which clearly makes it a low-k material ($\varepsilon_r < 4$) ideally suited to application as an insulating layer in microelectronic devices. These results underline the possibilities of fine-tuning the mechanical and dielectric properties of silica thin films simply through control of the properties of the solution from which they are cast.

4. Conclusions

This paper presented a systematic investigation into the relationships between the structural/morphological features of colloidal casting solutions and the physical properties of the resulting silica thin films. Our objective was to formulate strategies for the preparation of stabilized casting solutions capable of producing optimized low-k (amorphous) silica thin films while maintaining precise control over particle size and phase features. In this study, we investigated two surfactants (TWEEN® 80 and Triton™ X-100), both of which contribute to the formation of uniform thin films with desirable mechanical and dielectric properties by enhancing the dispersion of nanoparticles (with a mean particle radius of ~10 nm) of high stability (exceeding 90 days). The underlying mechanisms of the two surfactants differ considerably. Triton™ X-100 resulted in solutions with fair nanoparticle dispersion, powders with moderate mesopore volume, and thin films with high mechanical strength. TWEEN® 80 has a longer main chain and bulkier side units, which led to micelle–nanoparticle coexisting dispersion (with a mean micelle size of approximately 200 nm), resulting in powders with high mesopore volume and thin films with a low dielectric constant (~3). The percolated, bi-continuous phase as has been noticed with the quenching thin film in the latter case is of particular interest, given its considerable potential in the fabrication of interconnected colloidal networks in solution or in quenching thin films using a minimum number of seed particles. The present findings demonstrate the possibility of fine-tuning the properties of low-k silica films by controlling the state of colloids in solution. The high-performance low-k silica films can be used in the electronic devices for reducing the signal delay and cross-talk noise.

Acknowledgements

C. C. C., A. C. Y. and D. Y. K. acknowledge financial support from the Ministry of Science and Technology (MOST) of Taiwan (MOST 104-2628-E-002-009-MY3 and MOST 105-2923-E-002-002-MY2) and National Taiwan University (NTU-CDP-105R7814). C. Y. S. and C. C. H. greatly appreciate financial support from the Ministry of Science and Technology of Taiwan (MOST 103-2221-E-194-059-MY3). All of the authors acknowledge technical support from U-Ser Jeng, Chun-Jen Su, Yi-Qi Yeh, Chun-Yu Chen,

This journal is © the Owner Societies 2016

Published on 29 June 2016. Downloaded by Synchrotron Radiation Library on 17/08/2016 02:19:24.

Wen-Bin Su, and Kuei-Fen Liao at beamline 23A in National Synchrotron Radiation Research Center of Taiwan. The valuable assistance of Cedric Po-Wen Chung and Hao-Ju Chou in the measurements of nitrogen physisorption is also acknowledged.

Notes and references

1 J. M. Gomez-Vega, M. Iyoshi, K. Y. Kim, A. Hozumi, H. Sugimura and O. Takai, *Thin Solid Films*, 2001, **398**, 615–620.
2 O. Wiltschka, D. Boecking, L. Miller, R. E. Brenner, C. Sahlgren and M. Linden, *Microporous Mesoporous Mater.*, 2014, **188**, 203–209.
3 X. Liu, Y. Hua and G. Villemure, *Microporous Mesoporous Mater.*, 2009, **117**, 317–325.
4 C. Y. Ting, H. S. Sheu, W. F. Wu and B. Z. Wan, *J. Electrochem. Soc.*, 2007, **154**, G1–G5.
5 S. Sakka and T. Yoko, *Chemistry, Spectroscopy and Applications of Sol-Gel Glasses*, Springer, Berlin Heidelberg, 1992, vol. 77, pp. 89–118.
6 J. D. Mackenzie and E. P. Bescher, *J. Sol–Gel Sci. Technol.*, 2000, **19**, 23–29.
7 T. Tsuru, T. Sudou, S. Kawahara, T. Yoshioka and M. Asaeda, *J. Colloid Interface Sci.*, 2000, **228**, 292–296.
8 T. Tsuru, *Sep. Purif. Methods*, 2001, **30**, 191–220.
9 T. Tsuru, M. Miyawaki, H. Kondo, T. Yoshioka and M. Asaeda, *Sep. Purif. Technol.*, 2003, **32**, 105–109.
10 H. L. Castricum, A. Sah, R. Kreiter, D. H. A. Blank, J. F. Vente and J. E. ten Elshof, *Chem. Commun.*, 2008, 1103–1105, DOI: 10.1039/b718082a.
11 T. Tsuru, *J. Sol–Gel Sci. Technol.*, 2008, **46**, 349–361.
12 H. L. Castricum, G. G. Paradis, M. C. Mittelmeijer-Hazeleger, R. Kreiter, J. F. Vente and J. E. ten Elshof, *Adv. Funct. Mater.*, 2011, **21**, 2319–2329.
13 T. Tsuru, A. Sasaki, M. Kanezashi and T. Yoshioka, *AIChE J.*, 2011, **57**, 2079–2089.
14 N. K. Raman, M. T. Anderson and C. J. Brinker, *Chem. Mater.*, 1996, **8**, 1682–1701.
15 T. Brennan, S. J. Roser, S. Mann and K. J. Edler, *Chem. Mater.*, 2002, **14**, 4292–4299.
16 A. M. Dattelbaum, M. L. Amweg, J. D. Ruiz, L. E. Ecke, A. P. Shreve and A. N. Parikh, *J. Phys. Chem. B*, 2005, **109**, 14551–14556.
17 Y. Horiuchi, H. Ura, T. Kamegawa, K. Mori and H. Yamashita, *J. Mater. Chem.*, 2011, **21**, 236–241.
18 S. Bian, H. Wu, X. Jiang, Y. Long and Y. Chen, *Prog. Chem.*, 2014, **26**, 1352–1360.
19 K. Kambara, N. Shimura and M. Ogawa, *J. Ceram. Soc. Jpn.*, 2007, **115**, 315–318.
20 M. Ogawa, K. Kato and N. Shimura, *Bull. Chem. Soc. Jpn.*, 2009, **82**, 121–125.
21 R. Hashimoto, M. Sato, N. Shimura, A. Ayral and M. Ogawa, *J. Ceram. Soc. Jpn.*, 2011, **119**, 867–871.
22 K. Yonaiyama, H. Saito, M. Higuchi, T. Asaka, K. Katayama and Y. Azuma, *J. Ceram. Soc. Jpn.*, 2003, **111**, 413–418.
23 K. Yonaiyama, H. Saito, M. Higuchi, K. Katayama and Y. Azuma, *J. Ceram. Soc. Jpn.*, 2004, **112**, 292–297.
24 G. Tan, C. Ford, V. T. John, J. He, G. L. McPherson and A. Bose, *Langmuir*, 2008, **24**, 1031–1036.
25 C. E. A. Kirschhock, R. Ravishankar, F. Verspeurt, P. J. Grobet, P. A. Jacobs and J. A. Martens, *J. Phys. Chem. B*, 1999, **103**, 4965–4971.
26 R. Ravishankar, C. E. A. Kirschhock, P. P. Knops-Gerrits, E. J. P. Feijen, P. J. Grobet, P. Vanoppen, F. C. De Schryver, G. Miehe, H. Fuess, B. J. Schoeman, P. A. Jacobs and J. A. Martens, *J. Phys. Chem. B*, 1999, **103**, 4960–4964.
27 S. Y. Yang and A. Navrotsky, *Chem. Mater.*, 2002, **14**, 2803–2811.
28 W. Fan, M. A. Snyder, S. Kumar, P.-S. Lee, W. C. Yoo, A. V. McCormick, R. L. Penn, A. Stein and M. Tsapatsis, *Nat. Mater.*, 2008, **7**, 984–991.
29 Y. Peng, H. Lu, Z. Wang and Y. Yan, *J. Mater. Chem. A*, 2014, **2**, 16093–16100.
30 S. Nagamine, K. Kurumada, M. Tanigaki and A. Endo, *Microporous Mesoporous Mater.*, 2001, **49**, 57–64.
31 S. B. Jung and H. H. Park, *Thin Solid Films*, 2006, **494**, 320–324.
32 Q. J. He, X. Z. Cui, F. M. Cui, L. M. Guo and J. L. Shi, *Microporous Mesoporous Mater.*, 2009, **117**, 609–616.
33 O. V. Shvets, N. Kasian, A. Zukal, J. Pinkas and J. Cejka, *Chem. Mater.*, 2010, **22**, 3482–3495.
34 S. H. Ye and S. G. Kim, *Korean J. Chem. Eng.*, 2010, **27**, 1316–1322.
35 M. N. Khan, S. M. Auerbach and P. A. Monson, *J. Phys. Chem. B*, 2014, **118**, 10989–10999.
36 M. K. Mardkhe, J. Lawson, B. Y. Huang, E. D. Handly and B. F. Woodfield, *Microporous Mesoporous Mater.*, 2015, **210**, 116–124.
37 Z. B. Wang, H. T. Wang, A. Mitra, L. M. Huang and Y. S. Yan, *Adv. Mater.*, 2001, **13**, 746–749.
38 S. Li, Z. J. Li and Y. S. Yan, *Adv. Mater.*, 2003, **15**, 1528–1531.
39 Z. J. Li, S. Li, H. M. Luo and Y. S. Yan, *Adv. Funct. Mater.*, 2004, **14**, 1019–1024.
40 S. Li, Z. J. Li, D. Medina, C. Lew and Y. S. Yan, *Chem. Mater.*, 2005, **17**, 1851–1854.
41 Z. J. Li, C. M. Lew, S. Li, D. I. Medina and Y. S. Yan, *J. Phys. Chem. B*, 2005, **109**, 8652–8658.
42 Z. L. Wang, J. J. Li, Z. H. Sun, Y. L. Li, Q. Luo, C. Z. Gu and Z. Cui, *Appl. Phys. Lett.*, 2007, 90.
43 S. Eslava, J. Urrutia, A. N. Busawon, M. R. Baklanov, F. Iacopi, S. Aldea, K. Maex, J. A. Martens and C. E. A. Kirschhock, *J. Am. Chem. Soc.*, 2008, **130**, 17528–17536.
44 S. Eslava, J. W. Seo, C. E. A. Kirschhock, M. R. Baklanov, K. Maex and J. A. Martens, *Adv. Funct. Mater.*, 2010, **20**, 2377–2379.
45 S. Eslava, L. Zhang, S. Esconjauregui, J. Yang, K. Vanstreels, M. R. Baklanov and E. Saiz, *Chem. Mater.*, 2013, **25**, 27–33.
46 Z. Li, M. C. Johnson, M. Sun, E. T. Ryan, D. J. Earl, W. Maichen, J. I. Martin, S. Li, C. M. Lew, J. Wang, M. W. Deem, M. E. Davis and Y. Yan, *Angew. Chem., Int. Ed.*, 2006, **45**, 6329–6332.
47 C. T. Tsai, H. Y. Lu, C. Y. Ting, W. F. Wu and B. Z. Wan, *Thin Solid Films*, 2009, **517**, 2039–2043.

Published on 29 June 2016. Downloaded by Synchrotron Radiation Library on 17/08/2016 02:19:24.

48 O. Larlus, S. Mintova, V. Valtchev, B. Jean, T. H. Metzger and T. Bein, *Appl. Surf. Sci.*, 2004, **226**, 155–160.
49 Y. Liu, C. M. Lew, M. W. Sun, R. Cai, J. L. Wang, G. Kloster, B. Boyanov and Y. S. Yan, *Angew. Chem., Int. Ed.*, 2009, **48**, 4777–4780.
50 Y. Liu, M. Sun, C. M. Lew, J. Wang and Y. Yan, *Adv. Funct. Mater.*, 2008, **18**, 1732–1738.
51 C. M. Lew, Z. Li, S. Li, S.-J. Hwang, Y. Liu, D. I. Medina, M. Sun, J. Wang, M. E. Davis and Y. Yan, *Adv. Funct. Mater.*, 2008, **18**, 3454–3460.
52 C. M. Lew, Y. Liu, B. Day, G. A. Kloster, H. Tiznado, M. Sun, F. Zaera, J. Wang and Y. Yan, *Langmuir*, 2009, **25**, 5039–5044.
53 Y. Kayaba, T. Sato, Y. Seino, T. Yamamoto and T. Kikkawa, *J. Phys. Chem. C*, 2011, **115**, 11569–11574.
54 H. K. Hunt, C. M. Lew, M. Sun, Y. Yan and M. E. Davis, *Microporous Mesoporous Mater.*, 2010, **128**, 12–18.
55 H. K. Hunt, C. M. Lew, M. Sun, Y. Yan and M. E. Davis, *Microporous Mesoporous Mater.*, 2010, **130**, 49–55.
56 M. E. Davis, *US Pat.*, 7109130, 2006.
57 A. Mitra, T. G. Cao, H. T. Wang, Z. B. Wang, L. M. Huang, S. Li, Z. J. Li and Y. S. Yan, *Ind. Eng. Chem. Res.*, 2004, **43**, 2946–2949.
58 D. I. Medina, *High-silica-zeolite BEA Spin-on Low-k Dielectric Films for Future Generation Computer Chips*, University of California, Riverside, 2005.
59 M. Johnson, Z. Li, J. Wang and Y. Yan, *Thin Solid Films*, 2007, **515**, 3164–3170.
60 S. Eslava, M. R. Baklanov, A. V. Neimark, F. Iacopi, C. E. A. Kirschhock, K. Maex and J. A. Martens, *Adv. Mater.*, 2008, **20**, 3110–3116.
61 S. Eslava, C. E. A. Kirschhock, S. Aldea, M. R. Baklanov, F. Iacopi, K. Maex and J. A. Martens, *Microporous Mesoporous Mater.*, 2009, **118**, 458–466.
62 H. Y. Lu, C. L. Teng, C. W. Yu, Y. C. Liu and B. Z. Wan, *Ind. Eng. Chem. Res.*, 2010, **49**, 6279–6286.
63 H.-Y. Lu, C.-L. Teng, C.-H. Kung and B.-Z. Wan, *Ind. Eng. Chem. Res.*, 2011, **50**, 3265–3273.
64 H. Y. Lu, C. H. Kung and B. Z. Wan, *J. Taiwan Inst. Chem. Eng.*, 2012, **43**, 971–979.
65 T. Y. Li, C. Y. Chang and B. Z. Wan, *Thin Solid Films*, 2014, **562**, 513–518.
66 Y. H. Wen, P. C. Lin, C. C. Hua and S. A. Chen, *J. Phys. Chem. B*, 2011, **115**, 14369–14380.
67 R. H. Guo, C. H. Hsu, C. C. Hua and S. A. Chen, *J. Phys. Chem. B*, 2015, **119**, 3320–3331.
68 A. Siegert, *MIT Radiation Lab*, Report, 1943.
69 B. J. Berne and R. Pecora, *Dynamic light scattering: with applications to chemistry, biology, and physics*, Dover Publications, New York, 2000.
70 S. W. Provencher, *Comput. Phys. Commun.*, 1982, **27**, 213–227.
71 M. F. Cardinal, M. Lovino and D. L. Bernik, *Mater. Sci. Eng., C*, 2007, **27**, 75–79.
72 O. Joshi and J. McGuire, *Appl. Biochem. Biotechnol.*, 2009, **152**, 235–248.
73 E. Prouzet, F. Cot, G. Nabias, A. Larbot, P. Kooyman and T. J. Pinnavaia, *Chem. Mater.*, 1999, **11**, 1498–1503.
74 Y. Z. Khimyak and J. Klinowski, *J. Mater. Chem.*, 2000, **10**, 1847–1855.
75 D. M. Nevskaia, M. L. R. Cervantes, A. G. Ruíz and J. de Dios López González, *J. Chem. Technol. Biotechnol.*, 1995, **63**, 249–256.
76 B. J. Schoeman, J. Sterte and J.-E. Otterstedt, *J. Porous Mater.*, 1995, **1**, 185–198.
77 J. Cravillon, C. A. Schröder, R. Nayuk, J. Gummel, K. Huber and M. Wiebcke, *Angew. Chem.*, 2011, **123**, 8217–8221.
78 M. Kley, A. Kempter, V. Boyko and K. Huber, *Langmuir*, 2014, **30**, 12664–12674.
79 S. Saha, S. Springer, M. E. Schweinefuß, D. Pontoni, M. Wiebcke and K. Huber, *Cryst. Growth Des.*, 2016, **16**, 2002–2010.
80 A. Aerts, L. R. A. Follens, M. Haouas, T. P. Caremans, M.-A. Delsuc, B. Loppinet, J. Vermant, B. Goderis, F. Taulelle, J. A. Martens and C. E. A. Kirschhock, *Chem. Mater.*, 2007, **19**, 3448–3454.
81 L. R. A. Follens, A. Aerts, M. Haouas, T. P. Caremans, B. Loppinet, B. Goderis, J. Vermant, F. Taulelle, J. A. Martens and C. E. A. Kirschhock, *Phys. Chem. Chem. Phys.*, 2008, **10**, 5574–5583.
82 R. D. Koehler and E. W. Kaler, *Langmuir*, 1997, **13**, 2463–2470.
83 S. R. Kline and E. W. Kaler, *J. Chem. Phys.*, 1996, **105**, 3813–3822.
84 A. Zaccone, H. Wu, M. Lattuada and M. Morbidelli, *J. Phys. Chem. B*, 2008, **112**, 1976–1986.
85 R. Pool and P. G. Bolhuis, *Phys. Chem. Chem. Phys.*, 2010, **12**, 14789–14797.
86 W. W. Lukens, P. Schmidt-Winkel, D. Zhao, J. Feng and G. D. Stucky, *Langmuir*, 1999, **15**, 5403–5409.
87 A. Schmid, P. Scherl, S. P. Armes, C. A. Leite and F. Galembeck, *Macromolecules*, 2009, **42**, 3721–3728.
88 L. Yang, S. Zhou, G. Gu and L. Wu, *J. Appl. Polym. Sci.*, 2013, **129**, 1434–1445.
89 Z. Chen, Y. Zhang, Y. Liu, L. Duan, Z. Wang, C. Liu, Y. Li and P. He, *Prog. Org. Coat.*, 2015, **86**, 79–85.
90 Y. Wang, H. Wang, X. Meng and R. Chen, *Sol. Energy Mater. Sol. Cells*, 2014, **130**, 71–82.
91 K. González-Matheus, G. P. Leal and J. M. Asua, *Polymer*, 2015, **69**, 73–82.
92 J. Yuan and H. Qian, *J. Appl. Polym. Sci.*, 2015, **132**, 42003.

This journal is © the Owner Societies 2016